High-geometrical-resolution imaging of dislocations in SiC using monochromatic synchrotron topography

X. R. Huang
Advanced Photon Source, Argonne National Laboratory, Argonne, Illinois 60439, USA

D. R. Black
National Institute of Standards and Technology, Gaithersburg, Maryland 20899, USA

A. T. Macrander[a] and J. Maj
Advanced Photon Source, Argonne National Laboratory, Argonne, Illinois 60439, USA

Y. Chen and M. Dudley
Department of Materials Science and Engineering, Stony Brook University, Stony Brook, New York 11794-2275, USA

(Received 11 August 2007; accepted 25 October 2007; published online 4 December 2007)

We demonstrate high-geometrical-resolution imaging of dislocations in 4*H*-SiC by monochromatic synchrotron topography (but still under the "integrated wave" condition). In back-reflection topographs, 1*c* screw dislocation images are "magnified" to appear as well-defined circular white spots, while basal plane dislocations with opposite edge Burgers vector components exhibit two distinct kinds of contrast features. All the dislocation images are precisely described by ray-tracing simulations. This imaging technique provides an accurate, comprehensive, and nondestructive characterization tool, which is needed by current SiC researchers is used for industrial applications. It also provides a simple picture for understanding the mechanisms underlying synchrotron diffraction imaging of defects. © *2007 American Institute of Physics*. [DOI: 10.1063/1.2814032]

SiC is an important wide-bandgap semiconductor for a variety of applications.[1] However, SiC crystals generally contain various defects, such as dislocations, stacking faults (SFs), etc., among which "super-screw dislocations" (SSDs) with large Burgers vectors in multiples of the *c* lattice constant ($b=nc$, including $n=1$) have been a major problem since they produce large lattice distortions and are detrimental to SiC devices.[2] Although hollow-core SSDs (i.e., micropipes with $n>1$) have been remarkably reduced in recent years, the densities of 1*c* dislocations and basal plane dislocations (BPDs) are still in the range of 10^2-10^5 cm^{-2} in most SiC wafers. Consequently, the research interest has largely shifted to investigating 1*c* dislocations, BPDs, and BPD-related SFs,[3,4] but there remain a number of unsolved critical problems. To address these issues, it is crucial to develop or upgrade techniques for precisely visualizing these defects.

X-ray topography is a widely used method for characterizing SiC.[5–9] Here we demonstrate the capability of high-geometrical-resolution imaging of dislocations in SiC using monochromatic topography based on the Advanced Photon Source (APS), one of the third-generation synchrotrons. The experiments were carried out at the topography station at beamline 33-BM, APS with a symmetric Si (111) double-bounce monochromator.[10] The crystals studied were 2 or 3 in. 4*H*-SiC(0001) wafers with the surfaces offcut 8° toward $[11\bar{2}0]$. We mainly used back-reflection geometry with Bragg angle $\theta_B=80°$ for $000\underline{12}$ reflection (x-ray energy $E=7.5$ keV). The images were recorded on nuclear emulsion plates.

Figure 1(a) shows a magnified image from part of the $000\underline{12}$ topograph taken from a high-quality 4*H*-SiC crystal. Here the 1*c* screw dislocations are nearly perpendicular to the crystal surface and their images appear as sharp circular white spots. In Fig. 1(b), the SSD density is much higher, but each dislocation is still clearly discernible, except that some images are slightly distorted due to the overlap of neighboring dislocation strains.[7] (Using smaller imaging distances *L*, we can resolve dislocations at a density up to 10^6 cm^{-2} as the diameters of the dislocation image shrink while the geometrical resolution increases with reducing *L*.) The larger white spots in Fig. 1(b) correspond to micropipes (*M*). It is remarkable that a Burgers vector of only 1 nm produces a circular image with diameter $D\sim 20$ μm on the topograph.

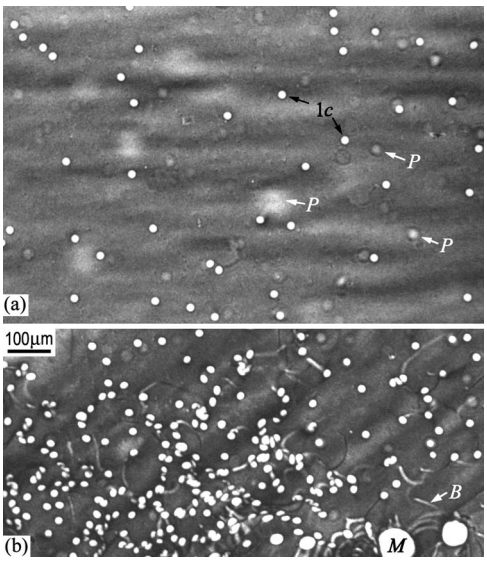

FIG. 1. Back-reflection images of 1*c* dislocations in 4*H*-SiC with densities 5×10^3 (a) and 7×10^4 cm^{-2} (b). Imaging distance $L=15$ cm. (*M*) micropipes, (*B*) BPDs, and (*P*) phase contrast images from defects of the beryllium windows used at the beamline.

[a]Electronic mail: macrander@aps.anl.gov

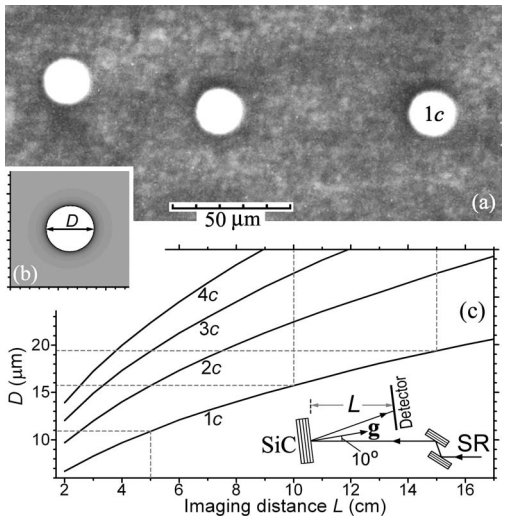

FIG. 2. (a) Magnified 1*c* dislocation images from Fig. 1(a). The diffraction intensity falls from maximum to zero across the periphery of the white center within 0.5 μm. (b) Simulated 1*c* image. (c) Variation of the image diameters D of SSDs with L. Inset shows the back-reflection geometry.

The contrast mechanism of 1*c* dislocations is that x rays diffracted from circular rings centered on the dislocation core form twisted cone-shaped ray bundles due to the helical lattice planes. The overlap of these cones on the detector then forms the circular images. This diffraction process can be simulated by the ray-tracing method, in which the distorted lattice is divided into small cubes that diffract x rays with the local diffraction vector $\mathbf{g}(\mathbf{r})=\mathbf{g}_0-\nabla[\mathbf{g}_0\cdot\mathbf{u}(\mathbf{r})]$, where $\mathbf{g}_0$ is the undistorted diffraction vector and $\mathbf{u}(\mathbf{r})$ is the lattice displacement field. Projecting the diffracted rays (with their phases and possible intensity variations ignored) along the local Bragg directions onto the detector yields the *orientation contrast*. The spreading of the diffracted rays leading to a "magnification" of the dislocation image.[6–8] The ray-tracing simulation has been used to simulate micropipe contrast, and in recent years it has been also applied to other defects.[5] However, in previous simulations of micropipe images,[6–8] the Burgers vector $b=nc$ was uncertain, so agreement between the simulated and recorded images was achieved by adjusting n. The clear images of 1*c* dislocations (with accurate Burgers vectors $b=c=1.005$ nm) in Fig. 2(b) provide a good opportunity to precisely test this mechanism.

Figure 2(b) shows the simulated image of a 1*c* dislocation based on a point source with a Gaussian-type spectrum ($\Delta\lambda/\lambda=1.5\times10^{-4}$), and the features indeed agree very well with those of the recorded images in Fig. 2(a). The calculated image diameter D is 19.4 μm while the measured value is 19.3 ± 0.5 μm for an imaging distance $L=15$ cm. Figure 2(c) shows the calculated dependence of D on L for the different Burgers vectors. In our experiments, the average values of D for 1*c* dislocations were also measured at $L=5$ and 10 cm and found to be 10.8 ± 0.3 and 15.6 ± 0.4 μm, respectively, which are again consistent with the calculated values of 11.0 and 15.8 μm.

Note that the diffracted wavelength slightly varies from point to point around the dislocation, but the variation is mostly within the bandwidth of the incident beam $\Delta\lambda/\lambda$ as verified in the ray-tracing simulation. Therefore, the "monochromatic-beam topography" here is still under the integrated-wave condition with the incident bandpass ($\approx$1.1 eV) much wider than the intrinsic Darwin curve width ($\approx$60 meV for 00012 reflection). This is different from "plane-wave topography" with the bandpass narrower than the Darwin width.[11] Nevertheless, the bandpass here is much narrower than a white beam, so it yields a significantly better signal-to-noise ratio.

In simulating Fig. 2(b), we have assumed a point source. It was found during the simulation that when the point source is shifted by Δz along directions perpendicular to the x-ray beam, the dislocation image is also displaced by $\Delta zL/L_s$ (thus blurring the overall image), where L is the imaging distance from the sample and L_s is the source-to-sample distance. For a finite source size D_s, this effect leads to the *geometrical resolution* D_sL/L_s.[11] Although the overall resolution of x-ray topography also depends on the detector resolution (grain size <1 μm for the nuclear emulsion plates) and the diffraction-spread effect (or dynamical diffraction effect), here the geometrical resolutions are significantly enhanced to $D_sL/L_s\sim0.3$ and 0.1 μm for imaging distances $L=15$ and 5 cm, respectively, based on the small effective source size ($D_s\sim100$ μm) and the long source-to-sample distance ($L_s\sim50$ m). In fact, the extremely small ratio D_s/L_s for third-generation synchrotrons enables one to "magnify" defect images using large imaging distance L (up to meters) without substantial blurring of the image details.[8,11–14]

Based on the ray-tracing principle, it is apparent that the dislocation image diffracted from a deep layer in the crystal will be slightly displaced from that of the surface layer since the diffracted beam is inclined from [0001].[7] Figure 2(b) is based on the diffraction contribution from a thin surface layer, which is reasonable as the penetration depth of 00012 reflection is ~3 μm (while the harmonics were largely suppressed). For white-beam topography, however, the harmonics with higher energy are fully activated and can penetrate the crystal more deeply, thus noticeably blurring the dislocation images (the diffraction-spread effects of different harmonics are also different).[7] Indeed, the sharpness of the dislocation images taken with reflections 00016 ($E=10$ keV), 00020 ($E=12.5$ keV), and 00024 ($E=15$ keV) does decrease with increasing E. This is another difference between "monochromatic-" and white-beam topography.

The ray-tracing method can also be used to examine BPD contrast. Figure 3(a) is a back-reflection topograph taken from a 4*H*-SiC crystal with a 2 μm homoepilayer grown on it. Here, in addition to the 1*c* dislocation images, the white and black lines are images of BPDs (mainly in the epilayer). The formation of BPDs is due to the fact that the energy difference between different stacking sequences of SiC is extremely small. So the lattice can easily slip on the (0001) basal planes, resulting in BPDs that are either perfect dislocations with Burgers vectors $\mathbf{b}=1/3\langle11\bar{2}0\rangle$ ($|\mathbf{b}|=0.31$ nm) or partial dislocations bounding SFs. Since gliding BPDs can be pinned by SSDs, most BPDs in Fig. 3(a) are connected to the SSDs. Due to the 8° offcut, some of the BPDs terminate at the crystal surface so that they appear as dislocation segments.

One can unambiguously identify two kinds of BPD contrast in Fig. 3(a). Nearly half of the BPDs appear as white stripes (B_+) with the widths ranging from 5 to 15 μm. The other half appear as narrow black lines (B_-) about 1–3 μm wide. The gliding BPD generally has an edge Burgers vector

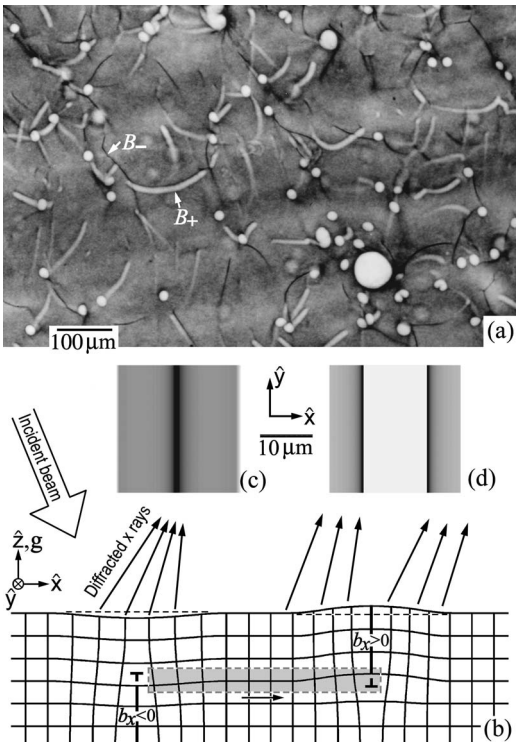

FIG. 3. (a) Two kinds of BPD contrast in back-reflection topograph. $L=12.5$ cm. (b) Contrast mechanisms of edge-type dislocations with opposite Burgers vectors. (c) and (d) are the simulated images of edge dislocations with $b_x=-0.31$ and 0.31 nm, respectively.

component $b_x=\mathbf{b}\cdot\hat{\mathbf{x}}$ (to relieve the local stresses), where $\hat{\mathbf{x}}$ is a unit vector perpendicular to the local dislocation line [Fig. 3(b)]. This component yields not only the major in-plane displacement field u_x that does not produce contrast, but also a vertical displacement $u_z=b_x[(1-2\nu)\ln r^2+(x^2-z^2)/r^2]/[8\pi(\nu-1)]$, where $r^2=x^2+z^2$ and ν is Poisson's ratio.[15] As schematically shown in Fig. 3(b), for $b_x>0$ (the extra half plane being above the BPD core), the u_z component distorts the (0001) basal planes into convex defocusing "mirrors." For $b_x<0$, the basal planes become concave focusing mirrors.

Obviously, the concave basal planes tend to focus the diffracted x rays into a narrow black line on the detector, while the convex planes give rise to a white stripe with the defocused x rays overlapping beside the stripe.[13,14] The focusing and defocusing patterns of Figs. 3(c) and 3(d) simulated by the ray-tracing method quantitatively confirm these effects. Since the BPD image width is proportional to $|\mathbf{b}\cdot\hat{\mathbf{x}}|$, it varies for different $\mathbf{b}$ or line directions of the BPDs, as can be seen from the various BPD widths.

The capability of identifying the sign of b_x is of practical importance. First, one can deduce the lattice slip directions from the directions of the dislocations and their Burgers vectors. For example, if we considered the two dislocations in Fig. 3(b) as a dislocation pair generated by the slip of the shaded local lattice, the slip is obviously toward $+x$ (starting from the $b_x<0$ dislocation) based on the signs of the two b_x's. Otherwise, if the slip is toward $-x$, the signs of the two b_x's will be reversed. Using back-reflection imaging, one can easily identify these two configurations. This capability is particularly powerful for either *in situ* or *ex situ* observations of nucleation and gliding of BPDs and related SFs in SiC *p-i-n* diodes, which is another severe problem for SiC devices.[3,4] Second, back reflection can be used to image general misfit dislocations in heterostructures, where the unambiguous determination of the edge Burgers vector directions can give detailed information about misfit strain relaxation. Here the advantage of the back-reflection geometry is that its resolution is higher than that of the commonly used grazing-incidence geometry.[10]

In our experiments, we also used asymmetric reflections to clearly image threading edge dislocations (TEDs), including the conversion of BPDs into TEDs during SiC homoepitaxy and the alignment of TEDs into dislocation walls (grain boundaries) in bulk SiC. These results will be presented elsewhere.

We appreciate the support and encouragement of Gabrielle G. Long, and we acknowledge the support of the XOR/UNI-CAT staff. The XOR/UNI-CAT facility is supported by the U.S. Department of Energy under Award No. DEFG02-91ER45439. The APS is supported by the U.S. Department of Energy, Office of Science, Office of Basic Energy Sciences, under Contract No. DE-AC02-06CH11357.

[1] P. G. Neudeck, in *The VLSI Handbook*, The Electrical Engineering Handbook Series, edited by W.-K. Chen (CRC/IEEE, Boca Raton, FL, 2000), p. 6.1.
[2] P. G. Neudeck, W. Huang, and M. Dudley, IEEE Trans. Electron Devices **46**, 478 (1999).
[3] S. Ha, M. Skowronski, J. J. Sumakeris, M. J. Paisley, and M. K. Das, Phys. Rev. Lett. **92**, 175504 (2004).
[4] X. Zhang, S. Ha, Y. Hanlumnyang, C. H. Chou, V. Rodriguez, M. Skowronski, J. J. Sumakeris, M. J. Paisley, and M. J. O'Loughlin, J. Appl. Phys. **101**, 053517 (2007).
[5] I. Kamata, H. Tsuchida, W. M. Vetter, and M. Dudley, J. Mater. Res. **22**, 845 (2007).
[6] X. R. Huang, M. Dudley, W. M. Vetter, W. Huang, S. Wang, and C. H. Carter, Jr., Appl. Phys. Lett. **74**, 353 (1999).
[7] X. R. Huang, M. Dudley, W. M. Vetter, W. Huang, W. Si, and C. H. Carter, Jr., J. Appl. Crystallogr. **32**, 516 (1999).
[8] J. Härtwig, J. Baruchel, H. Kuhn, X. R. Huang, M. Dudley, and E. Pernot, Nucl. Instrum. Methods Phys. Res. B **200**, 323 (2003).
[9] H. Jacobson, J. P. Bergman, C. Hallin, E. Janzén, T. Tuomi, and H. Lendenmann, J. Appl. Phys. **95**, 1485 (2004).
[10] D. R. Black, J. C. Woicik, M. Erdtmann, and T. A. Langdo, Appl. Phys. Lett. **88**, 224102 (2006).
[11] F. Zontone, L. Mancini, R. Barrett, J. Baruchel, J. Härtwig, and Y. Epelboin, J. Synchrotron Radiat. **3**, 173 (1996).
[12] R. Barrett, J. Baruchel, J. Hartwig, and F. Zontone, J. Phys. D **28**, A250 (1995).
[13] I. Matsouli, V. Kvardakov, J. Espeso, L. Chabert, and J. Baruchel, J. Phys. D **31**, 1478 (1998).
[14] J. Härtwig, S. Köhler, W. Ludwig, H. Moriceau, M. Ohler, and E. Prieur, Cryst. Res. Technol. **37**, 705 (2002).
[15] J. P. Hirth and J. Lothe, *Theory of Dislocations* (Wiley, New York, 1982), p. 78.